Journal of Manufacturing Processes 106 (2023) 537–551

Contents lists available at ScienceDirect

Journal of Manufacturing Processes

journal homepage: www.elsevier.com/locate/manpro

On the transition of failure mechanisms during machining process with varied speeds: A molecular dynamics study

J.Q. Zhang, B.B. He *, B. Zhang *

Department of Mechanical and Energy Engineering, Southern University of Science and Technology, Shenzhen 518055, China

ARTICLE INFO

Keywords:
Ultra-high-speed machining
Molecular dynamic simulation
Adiabatic shear banding
Shock wave

ABSTRACT

Conventional machining theory states that the machining of a ductile material may create continuous, serrated, and/or fragmented chips with increasing machining speeds. In this study, transitions of failure mode under varied machining speeds in single-crystalline silicon were analyzed based on molecular dynamics (MD) simulations of the ultra-high-speed machining of single-crystalline silicon. The MD simulations employ the periodic boundary conditions along the third direction which can mimic the material failure in cutting plane. The uncut depth reaches 39 nm, which is sufficiently large to accommodate complex atomic evolutions. The simulation results indicate that jetted chips occurred in front of the cutter, when the machining speed is increased to approximately 2.7×10^3 m/s, which is attributed to the shock pressure induced by the chip inertia. Essentially, the Rankine-Hugoniot jump conditions were introduced to explain the influence of the shock pressure. Both the calculations based on Rankine-Hugoniot jump conditions and the MD results imply that the shock wave speed is equal to the machining speed at the steady machining state. In addition, the transition from fragmented-chip to jetted-chip morphology exhibits a stage wherein the two primary adiabatic shear bands are simultaneously activated. The present work sheds light on the underlying mechanism of chip formation at an ultra-high-machining speed beyond 1000 m/s.

1. Introduction

In the previous studies, high-speed machining (HSM) incurred conventional failure modes, namely, the adiabatic shear band (ASB) which is intrinsically induced by material instability and is prevalent in HSMs of ductile materials [1]. With increasing machining speeds, the morphology of chips changes from continuous to serrated and further to fragmented [2–5]. However, it is unclear whether fragmented chips are the final morphology. Various scholars have conducted studies on chip morphology to investigate the final morphology of chips. Molinari [6] reported that chip morphology changes from fragmented to continuous in the results of finite element analysis (FEA) of a Ti6Al4V material at a machining speed of 350 m/s, because the characteristic time of ASB onset to reach the free surface is longer than the characteristic time of chip-material convection. Essentially, an ASB does not have sufficient time to grow and reach the free surface under ultra-high-speed machining (UHSM) conditions to form fragmented chips.

There are some limitations to the current FEA methodology that was used to simulate UHSM. First, when the machining speed is sufficiently high, the inertial effect induces high pressure. The current FEA simulations consider only the material shear behaviors governed by the deviatoric part of the stress tensor. Furthermore, the constitutive models that describe the material shear behaviors, including the Johnson-Cook model and Zerilli-Amstrong model [7–10], cannot predict the material deformation behavior due to shock pressure of UHSM. Second, the "element deletion" technique widely used in the current FEA simulations is not physical and may incur unrealistic localized stress in front of the cutter tip. The technique of "element deletion" requires configuring a layer of elements between the chip elements and bulk material elements. Such a layer of elements, also called the "separation layer" [5,11], is used to separate chip elements and bulk material elements. In most cases, the elements of the "separation layer" are assigned based on a relatively weaker damage criterion to ensure that the elements of the "separation layer" are deleted during the chip formation [6,9]. These simulations are not an accurate representation of the real-world scenarios, since the material of a single workpiece cannot satisfy two distinct damage criteria. Additionally, materials do not disappear during the machining process; in contrast, the materials represented by the

* Corresponding authors.
E-mail addresses: hebb@sustech.edu.cn (B.B. He), zhangb@sustech.edu.cn (B. Zhang).

https://doi.org/10.1016/j.jmapro.2023.09.064
Received 14 September 2022; Received in revised form 20 August 2023; Accepted 14 September 2023
Available online 17 October 2023

"separation layer" are deleted in the FEA simulations. Unrealistic stresses are another issue in "element deletion". The stress distributions surrounding the deleted element are singular and discontinuous. Although stress singularity and discontinuity do not seem to influence the evolution of chip morphology at relatively low machining speeds, under the machining speeds characteristic of UHMS, they may cause an unexpected chip morphology evolution. Molecular dynamics (MD) simulation is another powerful approach to UHSM simulations. However, the primary issue in the current MD simulations is the size scale. In the current simulation scales, the number of atoms involved in the MD simulations is too small and results in atomic piles in front of the cutter [12,13]. Therefore, it can be concluded that only a few simulations can reasonably predict valid failure modes for UHSM with machining speeds of the order of 10^3 m/s.

Presently, there are no widely recognized systematic frameworks to obtain the failure modes in UHSM; however, few efforts have been made in the past decades to establish such a framework. Salomon conjectured that the machining temperature would decrease beyond the maximum temperature point with increasing machining speeds [14]; however, this still remains controversial and has not been verified [15]. Furthermore, numerous experimental results have shown that the Salomon's conjecture may be incorrect [16,17]. In 2003, Zhou et al. [18] proposed that the plastic wave speed decreases with increasing machining speeds. Similar results were reported by Wang et al. [19]. Furthermore, it has been concluded that when the machining speed attains critical speed, the plastic wave speed exceeds the machining speed, which results in brittle fractures in the ductile workpiece. Note that because the failure mode transitions from plastic deformation to brittle fracture, the plastic work does not contribute to the heat and the machining temperature decreases. These conclusions agree with the temperature drop conjectured by Salomon. However, these conclusions were based on the stress–strain curve of tensile testing of a ductile material, wherein the deformation was governed by shear stress. However, the material in front of the cutter was governed by the shock pressure when the machining speed is extremely high (10^3 m/s). Theoretically, the process of a material experiencing a shock is treated as a discontinuous process that can be described by the Rankine-Hugoniot jump conditions combined with the equation of state (EOS) [20].

This study explores the evolution of the material failure mode of single-crystalline silicon (SCS) machined in the "ductile regime" mode with increasing machining speeds ranging from 200 m/s to 8800 m/s. To avoid stress singularity and artificial "separation layer" in the FEA, MD simulations were conducted to obtain optimal and detailed descriptions of the material failure modes. The simulation yielded the following findings. First, microvoids were observed within the ASB. Second, the relationship between the characteristic times of the primary ASB growth and the material convection was not only competitive but also sequential. Third, the simultaneous activation of the two primary ASBs was the key mechanism for the transition from shear triggering to pressure triggering. As the machining speed was increased further, the two primary ASBs were suppressed by the pressure induced by the atom inertia. Fourth, jetted chips were formed when the pressure induced by the shock wave governed the failure mode. The shock wave speed was proved to be equal to the machining speed at the steady machining stage using the Rankine-Hugoniot jump condition and the simulation results. The pressure induced by the shock might also result in several other phenomena, including bifurcations and the wavy shape of the primary ASBs.

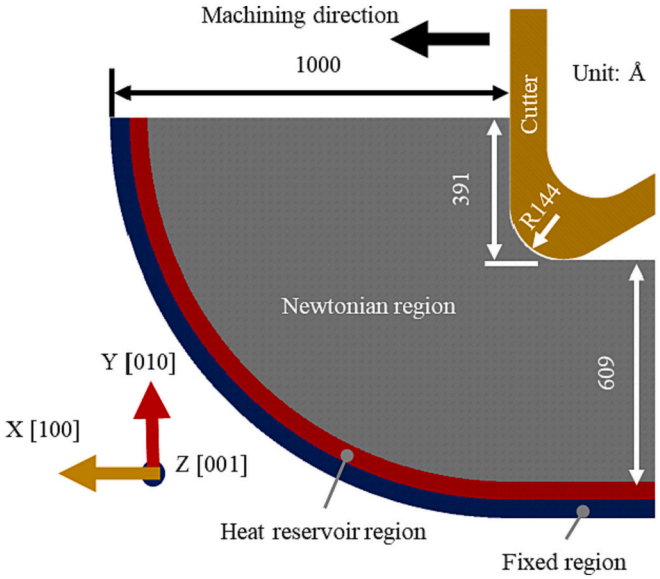

Fig. 1. Configurations of molecular dynamics in UHSM of CSC.

2. Methodologies

2.1. Modeling configurations

A molecular dynamic model was built at the nanometer scale to simulate the orthogonal machining, as Fig. 1. The overall dimensions of the workpiece were approximately 1000 × 1000 Å^2 in the X-Y plane. Because the machining force generated by the orthogonal machining lied only on the X-Y plane [16], periodic boundary conditions were imposed on the atoms at the two sides of the model. Owing to the workpiece under compression in X-Y plane in machining, the compressed atoms have a trend to move beyond the two sides normal to the Z direction. Nevertheless, the periodic boundary condition requires that if an atom moves beyond one side, it will enter into the boundary from the opposite side, which implies the normal strain along Z direction is always zero. Therefore, periodic boundary condition is equivalent to the plane strain assumption in the FEA simulation of the HSM. Significant dimensions, including the cutter nose radius and uncut depth, are labeled in Fig. 1. The entire workpiece was divided into three regions: Newtonian, heat reservoir, and fixed regions. The Newtonian region simulated the material deformation behavior under machining; the heat reservoir region provided heat to the model; and the fixed region was used for imposing the fixed boundary conditions. The total number of atoms in the three regions was 841,008. The crystallographic orientations of [100], [010], and [001] of the workpiece were along the X, Y, and Z axes, respectively (Fig. 1). A diamond cutter in the model was assumed to be a rigid body. Before machining, relaxation was performed to ensure that the workpiece was maintained at room temperature (298 K). During relaxation, the Newtonian region was treated as a microcanonical ensemble, and initial energy minimization was conducted. Subsequently, the method proposed by Berendsen et al. [21] was applied to couple the atoms in the heat reservoir region and the atoms in the Newtonian region to stabilize the workpiece at the specified temperature. Both the energy minimization and coupling processes were repeated for 7000 cycles, at least, until the workpiece attained the room temperature. After relaxation, the cutter was slid along the negative direction of the X-axis for machining under the fixed boundary conditions. The simulations were conducted by the open-source software LAMMPS with a post-process by the software OVITO.

In this study, the primary focus was on the material failure modes that vary with machining speeds. Eight cases (Case 1–8) were respectively studied at the respective machining speeds: 200, 1086, 1300, 2000, 2715, 4073, 5431, and 8800 m/s. These machining speeds were selected to cover the machining speed range corresponding to the shear-triggering failure mode and pressure-triggering failure mode.

2.2. Calculation approaches employed in the simulations

In the MD simulation, the interactions among the silicon atoms can be defined using the Tersoff potential function [22], which is given by

$$\Phi = \frac{1}{2}\sum_{i}\sum_{j\neq i} f_C(r_{ij}+\delta)\left[f_R(r_{ij}+\delta) + b_{ij}f_A(r_{ij}+\delta)\right], \quad (1)$$

where f_C is the cut-off radius function; f_R is the repulsive potential term; b_{ij} is the bond order between atoms i and j; f_A is the attractive potential term; r_{ij} is the cut-off distance; and δ is an optional negative shift of the equilibrium bond length. The coefficients and parameters in the three-body Tersoff potential function were obtained from Tersoff's work [22]. This potential function defined the interactions among the atoms of the workpiece (Si—Si interactions) and the interactions between the cutter and the workpiece (Si—C interactions). The file used in MD defining the parameters of Tersoff potential function can be downloaded from the webpage of National Institute of Standards and Technology.

The stress, strain, and temperature fields obtained from the MD simulation exhibited discontinuous characteristics and had to be averaged to obtain smooth fields. The averaging method employed in this study is shown in Fig. 2. As the figure, the quantity at the central atom was averaged. The adjacent atoms were considered in the averaging process. All the atoms were assumed to be within a sphere with a cut-off radius for the averaging process. The average quantity at the central atom is given by

$$\alpha_{avg} = \frac{1}{N}\sum_{i=1}^{N}\alpha_i, \quad (2)$$

where α_i is the quantity of the ith atom; α_{avg} is the averaged quantity of the central atom; and N is the total number of atoms within the assumed spherical space. The cut-off radius used in this study was set to 4 or 8 Å to ensure smooth quantity fields.

The Green-Lagrangian strain tensor was adopted in this study to describe the large deformations of a solid. The Green-Lagrangian strain tensor is given by $E_{ij} = \frac{1}{2}(F_{ji}F_{ij} - \delta_{ij})$, where F_{ij} is the deformation gradient tensor; δ_{ij} is the Kronecker delta; and i and j are indices, which are assigned the values 1, 2, and 3 corresponding to the X, Y, and Z directions, respectively. The deformation gradient tensor is obtained from the atom locations and is given by $F_{ij} = \frac{\partial x_i}{\partial X_j}$. The equivalent strain at each atom used in the following sections is given by $\varepsilon_{atom} = \sqrt{\frac{2}{3}E_{ij}^{dev} : E_{ij}^{dev}}$, where E_{ij}^{dev} represents the deviatoric part of the strain tensor.

Virial stress is used to indicate the stress level. It is calculated using the superposition of the kinetic energy contribution and pairwise force contribution [23]. The virial stress is given by

$$\sigma_{ij} = -\frac{1}{V_a}\left[mv_iv_j + \frac{1}{2}\sum_{n=1}^{N}\left(r_{1i}P_{1j} + r_{2i}P_{2j}\right)\right], \quad (3)$$

where V_a is the space for averaging; m is the mass of the atom; r_1 and r_2 are the positions of a pair of neighbor atoms; and P_1 and P_2 are the forces of a pair of neighboring atoms. Because the workpiece was loaded by the cutter, the stress state of the workpiece usually had a negative hydrostatic part. For convenience, the pressure was utilized as an alternative to represent the negative hydrostatic stress; the pressure is given by $p = -\frac{\sigma_{11}+\sigma_{22}+\sigma_{33}}{3}$.

Temperature is another significant factor that influences the failure mode evolution in a shock. In this study, the temperature was calculated by averaging the kinetic energy of each atom. Thus, the temperature can be obtained using the following equation

$$T = \frac{\sum_{n=1}^{N} m\left(v_{n,x}^2 + v_{n,y}^2 + v_{n,z}^2\right)}{3NN_Ak_B}, \quad (4)$$

where $v_{n,x}$, $v_{n,y}$, and $v_{n,z}$ are the velocities of the nth atom along the X, Y, and Z directions, respectively; N is the total number of atoms within the spherical space; k_B is the Boltzmann constant; T is the average temperature of the central atom; and N_A is Avogadro's number. The atoms of the workpiece loaded by the cutter had translational mass-center velocities in the X-Y plane. The mass-center velocity did not contribute to heat generation; therefore, they were excluded from the temperature evaluation. Based on the reference MD shock simulations [24,25], it was assumed that the temperature was proportional to the atomic thermal motion along the Z-direction because the mass center velocity component along the Z-direction at some extents was not affected by the cutter loading. Then, Eq. (4) is modified as

$$T = \frac{\sum_{n=1}^{N} mv_{n,z}^2}{NN_Ak_B}. \quad (5)$$

The localized density of the workpiece was evaluated by the Voronoi tessellation method. In the simulations, the software package Voronoi++ (version 0.4.6) was used, which provided a cell-based Voronoi tessellation algorithm. The localized density of one atom was calculated by dividing the atomic mass by the tessellation volume occupied by the atom. The specific volume used in the following sections was calculated by inverting the density. Additionally, the algorithm, which was developed by Maras (2016) [26], was adopted in the simulations to identify cubic structures.

The radial-pair distribution function (RDF) was used to identify the amorphous structure. The RDF can be defined as [27]

$$g(r) = \frac{N(r+dr) - N(r)}{\rho_0(V(r+dr) - V(r))}, \quad (6)$$

where $N(r)$ and $N(r + dr)$ are the number of atoms within the spherical space with radius r and $r + dr$, respectively; ρ_0 is the density of the number of atoms in the bulk material; and $V(r)$ and $V(r + dr)$ are the volume of the spherical space with radius r and $r + dr$, respectively. When r increased to a larger number, the RDF of the amorphous structures approached 1; in contrast, even when r was a large number, the RDF of the crystalline structure was always in a periodic characteristic.

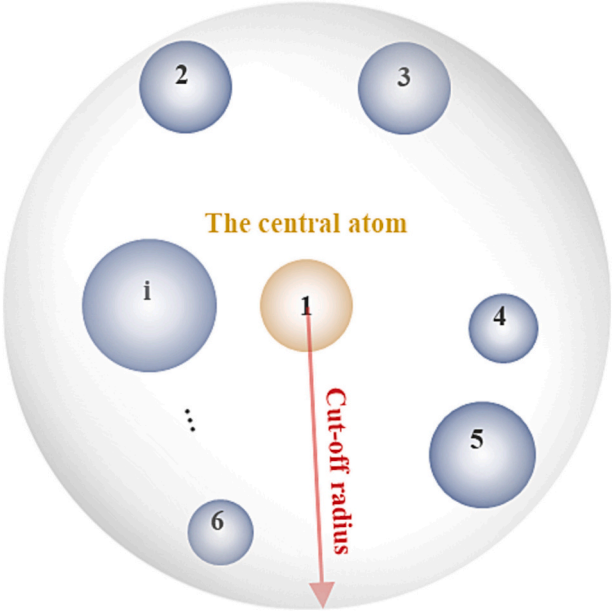

Fig. 2. Sphere for quantity averaging.

3. Results and discussion

3.1. Failure mode transition and corresponding metallurgical structure and temperature variations

3.1.1. Failure mode transition with machining speeds

Typical material failure modes at different machining speeds were represented by equivalent shear strain fields, as Fig. 3. The overall trend of the material failure mode changed from a heterogeneous failure mode to a homogeneous failure mode with increasing machining speeds. As Fig. 3(a), when the machining speed v_C was 200 m/s, a typical heterogeneous failure, i.e., the primary ASB, was active and propagated; consequently, the primary ASB caused a fragmented chip formation. When the machining speed v_C was elevated to 1086 m/s, the ASB became wavy and ASB bifurcations were observed, as Fig. 3(b). The bifurcation nucleated within the ASB and deviated from the primary ASB. When the machining speed was v_C = 1300 m/s, as Fig. 3(c), the second-primary ASB was active from the free-surface corner marked in Fig. 3(c). The two primary ASBs propagated and connected. The second-primary ASB prevented the primary ASB from propagating to the free surface and forming fragmented chips. At a high machining speed of 2715 m/s, the propagation of the two primary ASBs was suppressed, as Fig. 3(d). Additionally, several crossed minor ASBs nucleated in the high-pressure region surrounded by the two primary ASBs, as Fig. 3(i). The suppression of the primary ASBs and the occurrence of the high-pressure region showed that the material failure modes transitioned from shear failure to pressure failure. When machining speed was v_C = 5431 m/s, the two primary ASBs were almost eliminated, and the crossed minor ASBs also disappeared. The failure modes at high machining speeds were more homogeneous compared to the failure modes at lower machining speeds. These failure modes are illustrated as equivalent strain and pressure fields in the supplementary video.

Inertia was the root cause of the transition from the shear failure modes to the pressure failure modes, which can be inferred from the shift of the maximum-pressure location, as Figs. 3(f)–(j). Maximum pressures were observed under the cutter tip at the machining speeds of 200, 1086, and 1300 m/s. The pressure concentration can be attributed to the round shape of the cutter tip, because a common sense is that stresses usually concentrate at notches. When the machining speed reached 2715 m/s, the maximum pressure shifted to the atoms in front of the rake face; this can be attributed to the fact that the atoms in front of the rake face had higher inertial forces. The inertial forces were incurred by the acceleration of the atoms along the machining direction. The atoms in front of the rake face were accelerated to the machining speed in a short time; however, the atoms under the cutter tip were not accelerated to the machining speed because they were passed by the cutter in the machining process. Therefore, the acceleration of the atoms in front of the rake face was higher than that of the atoms under the cutter tip, which causes higher inertial force of the atoms in front of the rake face. Such inertial force is the origin of high pressure. When the machining speed was 5431 m/s, higher inertia causes higher localized pressure in front of the rake face.

The high pressure induced by the inertia in front of the rake face suppressed the two primary ASBs. Molinari et al. studied ASB suppression by pressure [6] and reported that inertia slowed down the strain concentration within the ASB because the high pressure induced by inertia confined the atom movement within the ASB and further impeded ASB propagation. In 2014, Cai et al. [28] experimentally verified that pressure can suppress ASB propagation. In the MD simulations, the pressure played an important role at a machining speed of 2715 m/s. The pressure on the atoms in front of the rake face suppressed the growth of the two primary ASBs and led to the separation of the primary ASBs, as Fig. 3(d). Additionally, when the machining speed was 2715 m/s, crossed minor ASBs were in the high-pressure region, which indicates that shear effects were still present in the high-pressure region.

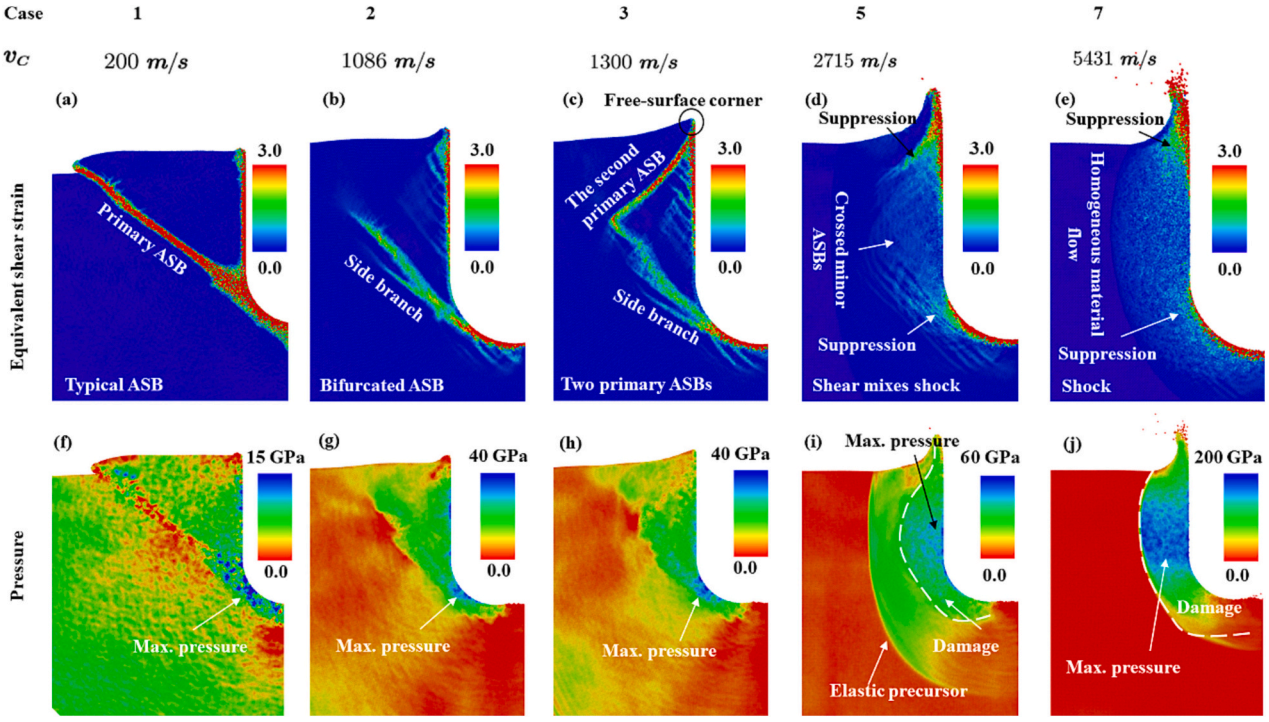

Fig. 3. Variation of the failure modes with machining speeds presented through equivalent shear strain fields. Five cases are selected under identical sliding distance (96 Å). The radius of the assumed sphere for equivalent strain field averaging was 4 Å, and that for pressure averaging was 8 Å. (a)–(d) represent the equivalent shear strain fields; (f)–(j) show the pressure fields. With increasing the machining speeds, the failure modes transit from shear-stress triggering to pressure triggering. Supplementary videos of three cases (Case 1, 3, and 7) were provided. (a), (f), (c), (h), (e), and (j) respectively corresponds to Video 1–6.

3.1.2. Metallurgical structures within ASB and the high-pressure region

To determine the metallurgical structure in the primary ASB and high-pressure region, a portion of the atoms of the damage region under the cutter tip at the machining speed of 200 m/s and in the high-pressure region at the machining speed of 5431 m/s were studied through RDF evaluation, as Figs. 4(a) and (b). The atoms for RDF evaluation were selected from a smaller region at a distance of at least 6 Å from the border of the damage region. In the cross-sectional view presented in Fig. 4(c), the selected atoms marked in red were within a band region with a thickness of 1 Å in the middle of the section. The radius of the assumed sphere for the RDF evaluation was set to 5.6 Å, which ensured that the diameter of the assumed sphere was smaller than the thickness of the model, 15.0 Å. This configuration ensured that there was no free space in the assumed sphere.

The results are shown in Fig. 4(d). The RDFs of the selected atoms at the machining speeds of 200 m/s and 5431 m/s are presented as Type 1 and Type 2, respectively. Moreover, the RDF of the crystalline structure is presented as Type 3. The first peaks of the three cases shared a distance of 2.52 Å, which is close to the published experimental results [29,30]. The RDF of Type 1 and Type 2 structure converged to 1 with an increase in the radius of the assumed sphere, which shows that a typical amorphous structure. In other words, the amorphous structure was transformed from the crystalline structure in the HSM and UHSM. This conclusion was also confirmed by Zhao [31]. Nevertheless, the RDF of the SCS had periodic features with an increase in the radius of the assumed sphere, as Type 3.

In the transformation from crystalline to amorphous, the Si—Si bond breaks to form dangling bonds. The existence of dangling bonds reduces the constraints to silicon atoms to benefit the formation of the microvoids in ASB that requires the surrounding atoms is of high flowability. The formation of the microvoids will be discussed in Section 3.2.2.

3.1.3. The temperature fields influenced by machining speeds

The virgin materials experienced high stress or pressure for a period of few picoseconds. As the period was very short, it can be assumed that the heat transfer was limited and all of the heat was provided by the work of the machining. Concerning the work-heat conversion efficiency, the heat at one material point can be obtained using the following equations

$$Q = \beta\left(\tau_{eq}\gamma_{eq} + p\varepsilon_V\right), \tag{7}$$

where Q denotes the generated heat; β is the Taylor-Quinney coefficient; τ_{eq} is the shear stress; γ_{eq} is the equivalent shear strain; ε_V is the volumetric strain. Eq. (7) indicates that the heat can be divided into two parts: the first part is incurred by shear stress, and the second part originates from the pressure. Nevertheless, in the simulation, it was observed that the two parts played significant roles in different machining speed ranges. For machining speeds lower than 1300 m/s, the heat was primarily created by the shear stress that accumulated within the ASBs, as Fig. 5(a). When the machining speeds were higher than 4073 m/s, the high temperatures were primarily created by the pressure, which was concentrated in the high-pressure region. The cases

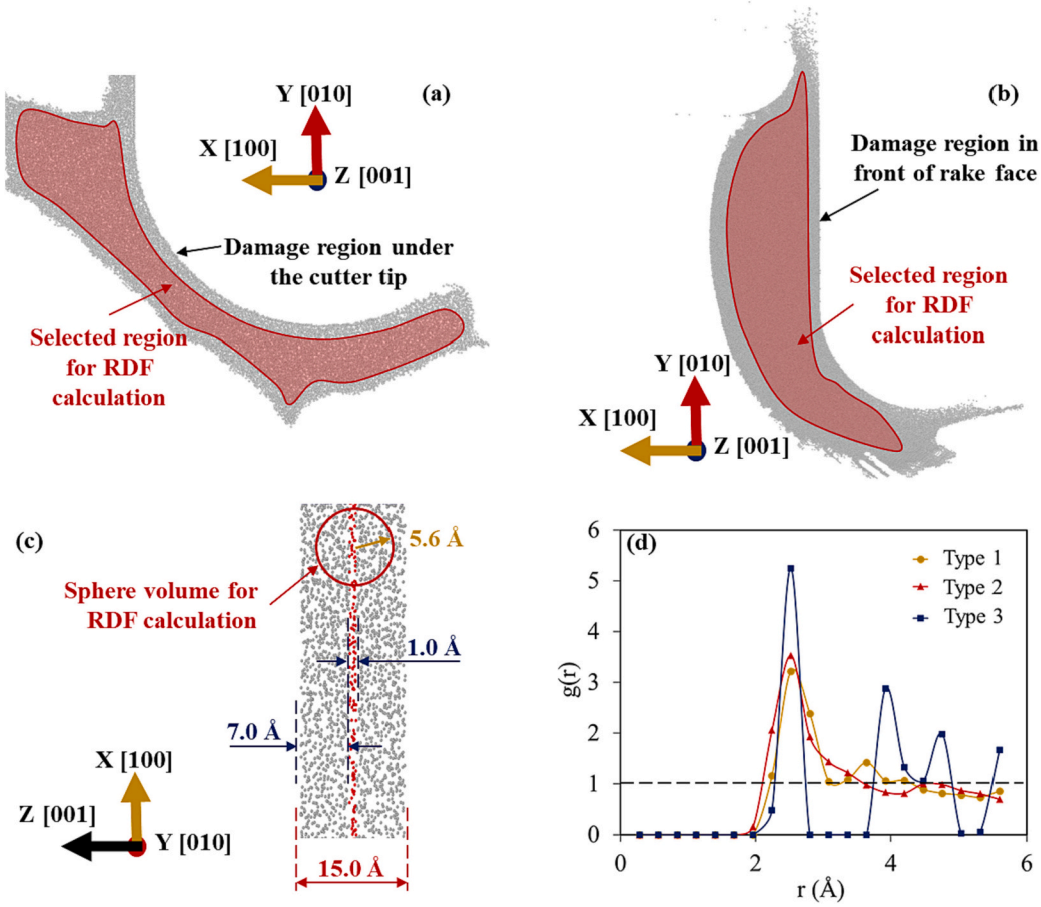

Fig. 4. RDF of amorphous and crystalline structure; (a) and (b) show the regions of the selected atoms viewed from the Z-direction; (a) shows the amorphous structure under the cutter tip at a machining speed of 200 m/s; (b) shows the amorphous structure in front of the rake face at a machining speed of 5431 m/s; (c) shows the band region of the selected atoms viewed from the Y-direction; (d) displays the RDF of the amorphous and crystalline structure. Type 1 and Type 2 represent the RDF at machining speeds of 200 m/s and 5431 m/s, respectively; Type 3 represents the RDF of SCS. Type 2 and 3 are convergent to 1 with increasing the radius of the assumed sphere implying Type 2 and 3 are the amorphous structure.

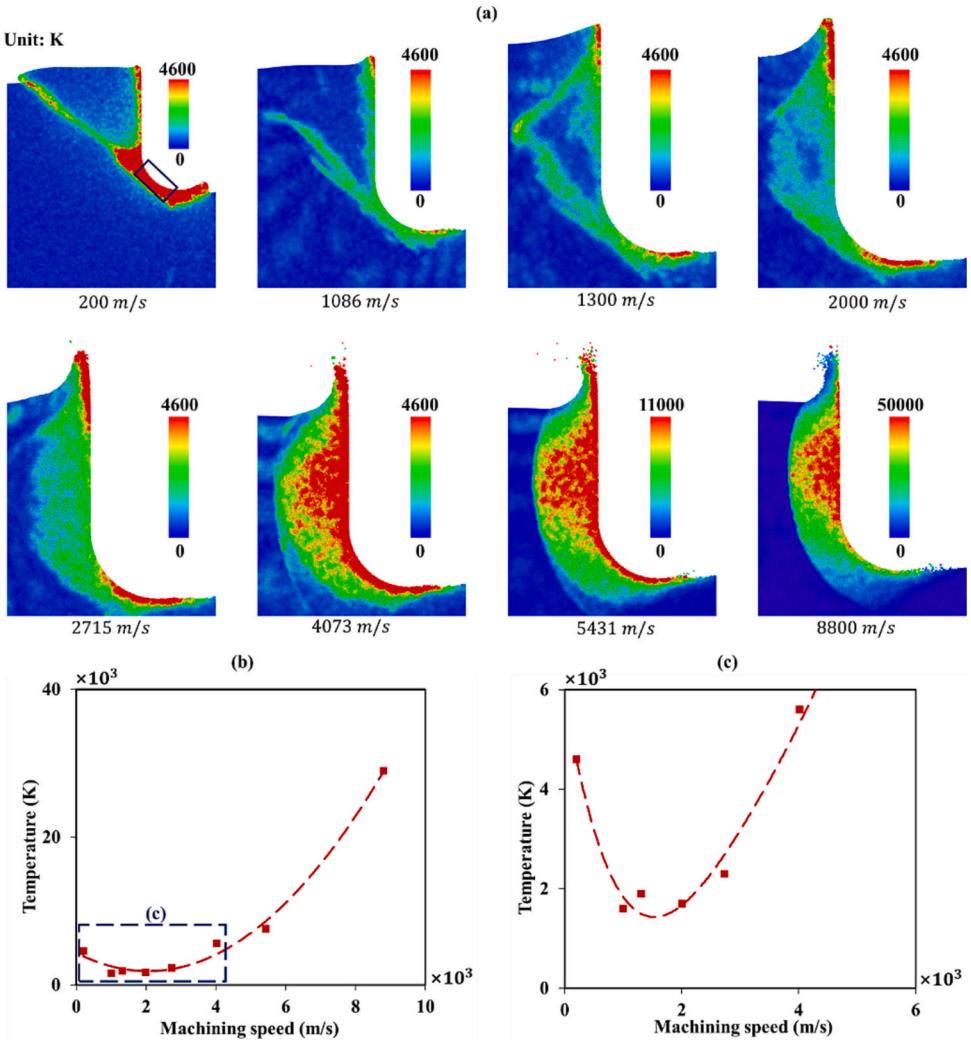

Fig. 5. Variation of temperature distribution with machining speeds; (a) shows the variation of the temperature fields with machining speeds. All cases were evaluated under the condition of the cutter sliding by 96 Å; a rectangle region was selected as the location for the temperature measurement under the cutter tip marked in the case of $v_C = 200$ m/s; the cut-off radius of the assumed sphere for temperature averaging was 8 Å; (b) displays the variation of the temperature under the cutter tip with machining speeds; (c) displays the local region of (b). The overall trend of temperature increases with enhancing in machining speeds. When the machining speed is higher than 4073 m/s, the work done by the pressure should be the major factor contributing to the temperature increase.

of machining speeds of 2000 m/s and 2715 m/s were of the feature transitioning from the heat within the ASB to the heat within the high-pressure region because high temperatures existed in both the high-pressure region and within the ASBs.

Overall, the temperature under the cutter tip increased with increasing machining speeds, as Fig. 5(b). The temperature under the cutter tip decreased significantly with increasing machining speeds in the range of 200–1300 m/s. In this range, the shear stress governed the material failure mode, as Fig. 5(c). Based on Eq. (7), it can be assumed that when the shear stress governed the material failure mode, heat was primarily generated from the work done by the shear stress within the primary ASBs. The shear stresses within the primary ASBs at the machining speeds of 200 m/s, 1086 m/s, and 1300 m/s were comparable. However, the equivalent shear strain within the ASB at the machining speed of $v_C = 200$ m/s was twice the shear strain in the other cases. The equivalent shear strain was the accumulation of the equivalent strain rate over time and can be obtained as follows

$$\gamma = \int_{t_0}^{t_1} \dot{\gamma} dt, \tag{8}$$

where t_0 is the moment when the cutter comes in contact with the workpiece; and t_1 is the moment when the cutter slid by 96 Å. The duration between the two moments was termed δt. Because the temperature comparison was based on the fact that the cutter slid by 96 Å, the distinct machining speeds resulted in different δt in each case. The duration for a machining speed of 200 m/s was 48 ps; whereas, for machining speeds of 1086, 1300, 2000, and 2715 m/s, the duration ranged from 4.4 to 8.8 ps. The shear strain within the ASB was found to be twice the shear strain in the other four cases, because of the large time duration in the case of 200 m/s. A larger strain and comparable stress resulted in more plastic work, which generated more heat causing higher temperature under adiabatic condition in the case of machining speed of 200 m/s. For machining speeds of 2000 m/s and 2715 m/s, shear governing transited to pressure governing. Therefore, in Fig. 4(a), the high temperatures were located within the two ASBs and the high-pressure region. In the cases of the machining speed higher than 4073 m/s, the localized heat was primarily contributed by pressure. A higher pressure at higher machining speeds resulted in larger volumetric strain, which resulted in more work. Therefore, as Fig. 5(b), the localized temperature increased with increasing machining speed for the machining speeds of 4073, 5431, and 8800 m/s, which disagree with Salomon's conjecture. Theoretically, a typical adiabatic shock line in pressure-specific volume plot determines the volumetric work

monotonically increase with specific volume decreasing. The more plastic work at higher machining speeds converted to more heat triggering higher temperature.

3.2. The mechanism of failure modes governed by shear stress

3.2.1. The duration of material convection during ASB growth

The amorphous structure within the primary ASB under the conditions of $v_C = 200$ m/s are shown in Fig. 6. As Fig. 6(a), the primary ASB onset originated from the region under the cutter tip. The duration from ASB onset to reaching the free surface was 18 ps, as Figs. 6(a)–(c). After reaching the free surface, the primary ASB became wider, which was caused by the material convection [6,32] and amorphization of the adjacent crystalline. In addition, microvoids started to nucleate at 62 ps, as Fig. 6(d). Subsequently, the microvoids coalesced to form a crack, as Figs. 6(e) and (f).

Molinari et al. [6] proposed a mechanism wherein the disappearance of fragmented chips in UHSM was induced by the competition between the duration of the primary ASB propagation to the free surface, $t_{propagation}$, and the duration of the material convection of the primary ASB, $t_{convection}$. If $t_{convection} < t_{propagation}$, then the primary ASB does not have sufficient time to reach the free surface. Consequently, fragmented chips are not formed. This mechanism is based on the results of the FEA simulation on Ti6Al4V at the millimeter scale. Nevertheless, different situations were observed in the MD simulation of SCS machining on the nanometer scale. The relationship between the primary ASB propagation and material convection was not only purely competitive but also sequential, which can be validated through the observation of the primary ASB width before and after reaching the free surface. The primary ASB width at 39 ps was used as a reference. Before reaching the free surface, the primary ASB width increased by 23.8 %, as Fig. 6(c). Similarly, it increased by 528.5 % after reaching the free surface, as Fig. 6(f). Therefore, it can be concluded that the convection mainly occurred after the ASB reached the free surface. Thus, the disappearance of the fragmented chips in UHSM is not induced by the competition between the primary ASB propagation and the material convection with the primary ASB. Based on our MD simulations, it can be concluded that the disappearance of fragmented chips is caused by the occurrence of the second primary ASB, which will be discussed in Section 3.2.4.

3.2.2. The negative pressure around microvoids

The previous studies have shown that the ASB failure is incurred by the microvoid evolution [33], including growth and coalescence. Negative pressure was observed to be the trigger for the growth of voids. Rice and Tracy studied the relationship between the void growth rate and hydro stress [34,35] and concluded that the void growth depends on the mean hydrostatic stress in the far field. Similar results were obtained in MD simulations. The hydrostatic stress field at the moment of microvoid nucleation is shown in Fig. 7(a). It can be observed that the microvoids were surrounded by negative pressure. After 65.5 ps, the number of atoms with high pressure was less than the number of atoms present after 62.5 ps. However, after 65.5 ps, the microvoids started to coalesce. After 70 ps, the coalesced microvoids formed a crack, and the pressure magnitude around the microvoids decreased further to a lower level. Note that the coalescence of the microvoids not only causes cracks, but also results in dimples on the chip surface. The dimples were observed on the chip of surface of Ti6Al4V [36].

To quantitatively depict the pressure variation, the number of atoms with a negative pressure magnitude higher than 2 GPa was counted and plotted against time, as Fig. 7(d). The average diameters of the five largest voids are plotted against time in Fig. 7(d). In Fig. 7(d), the number of atoms with a magnitude of negative pressure larger than 2 GPa was the largest at 62.5 ps. Subsequently, the magnitude decreased with an increase in the average void diameter. After 64 ps, the growth

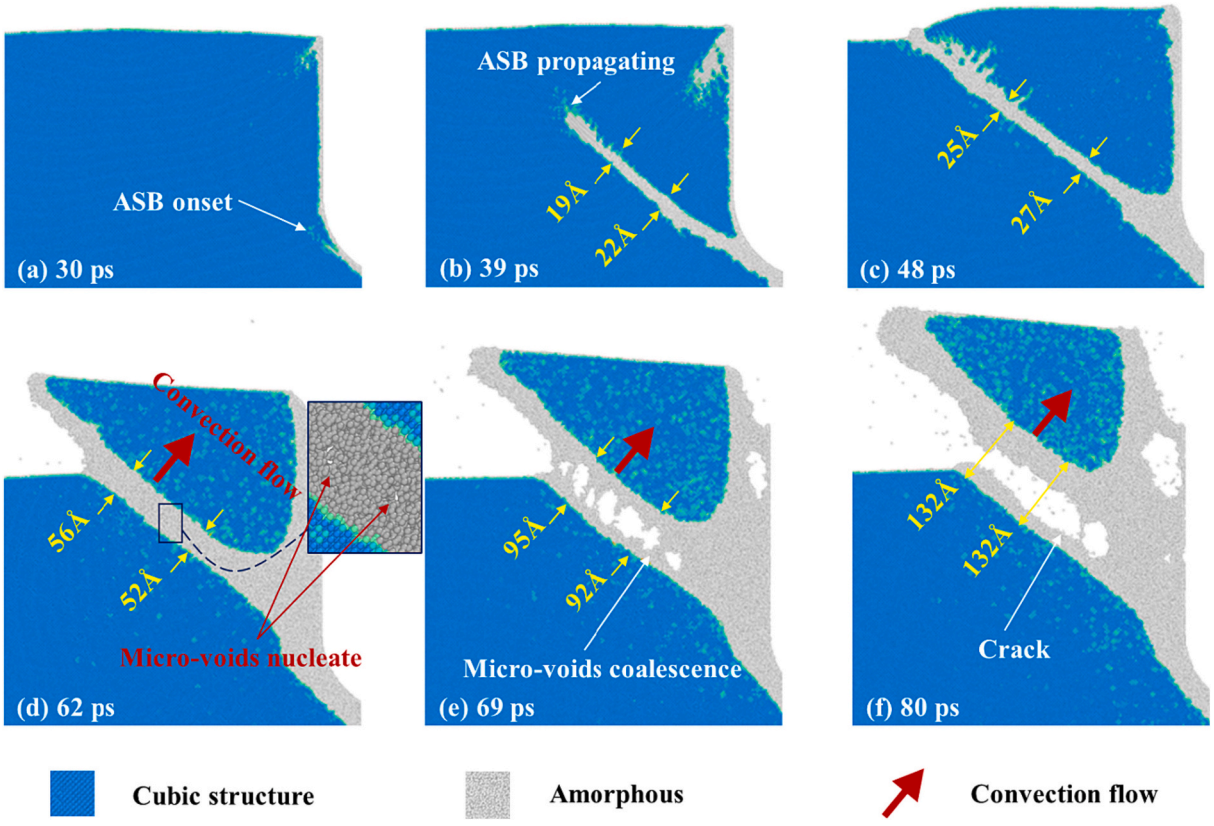

Fig. 6. The process of fragmented chip formation at the `machining speed of 200 m/s. The ASB propagation was followed by material convection flow. No obvious competition was observed between the ASB propagation and the material convection.

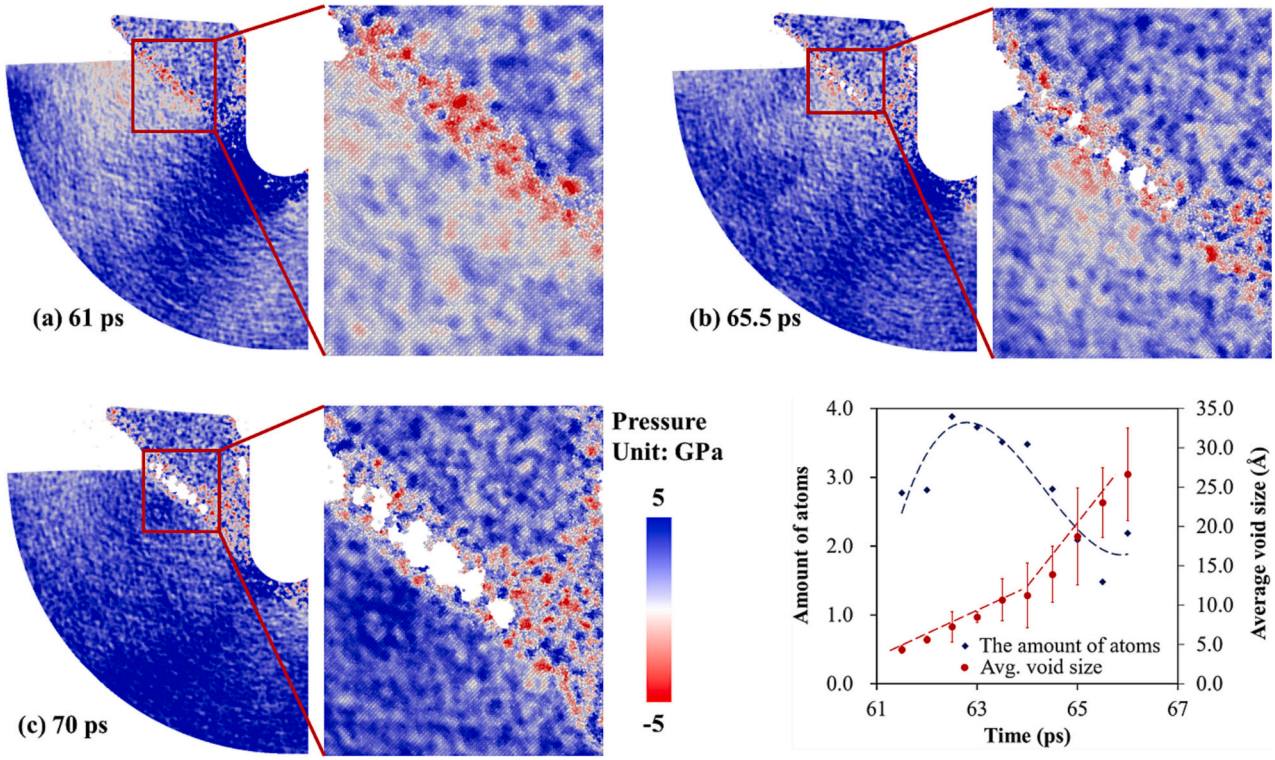

Fig. 7. Pressure around the voids within ASB; (a)–(c) show the pressure around the voids and the void sizes after 61, 65.5, and 70 ps; (d) shows the variation in the number of atoms with a magnitude of negative pressure larger than 2 GPa with time; (d) also shows the change in average void size with time. The negative pressure stretching the materials governs the growth of the microvoids.

rate of the microvoids accelerated, and the amount of the atoms of the pressure higher than 2 GPa decreases, which indicates that the strength of the material surrounding the microvoids decreased.

3.2.3. Disturbance in the primary ASB

Side branches were discovered in the primary ASB under the machining speeds of $v_C = 1086$ m/s and $v_C = 1300$ m/s, as Figs. 3(b) and (c), respectively. Because the propagation of ASBs was driven by shear stress, and the orientation of ASBs was related to the direction of the maximum shear stress, the nucleation of the side branch was driven by the maximum shear stress. Furthermore, the orientation was influenced by the direction of the maximum shear stress.

To study the influence of the maximum shear stress on the side-branch nucleation, statistical methods were applied to the maximum shear stress. The atoms within the side-branch nucleation were selected after 5.375 ps, 6.25 ps, and 8.125 ps, as Figs. 8(a-I), (b-I), and (c-I). The atoms for statistical analysis were filtered based on the condition that the von Mises values were greater than the stress thresholds. These thresholds and the number of atoms are presented in Figs. 8(a-II), (b-II), and (c-II). Additionally, the projection of the maximum shear stress direction of the atoms within the side branch on the X-Y plane was defined in Fig. (a-II); the angle between the projection on the X-Y plane and Y-axis was defined as the shear angle, which indicated the projection direction, as Fig. 8(a-II).

The distribution of the maximum shear stress is shown in Figs. 8(a-III), (b-III), and (c-III). The expectations of the distributions of the maximum shear stress fell in the ranges of 12.7–14.9 GPa, 16.9–19.4 GPa, and 19.1–22.1 GPa after 3.375 ps, 6.25 ps, and 8.125 ps, respectively; which shows that the expectations of the maximum shear stress increased in the side-branch nucleation. If the expectation of the maximum stress distribution was treated as a side-branch nucleation criterion, then the stress criteria would have fallen within the range of 12.7–22.1 GPa.

The shear angle distributions at the three moments are shown in Figs. 8(a-IV), (b-IV), and (c-IV). After 5.375 ps, the shear angle fell in the range of −27.1°–35.5°, and the peak occurred in the range of 8.7°–17.7°; after 6.25 ps, the shear angle fell in the range of −17.9°–18°, and the peak occurred in the range of 9.0°–18.0°; after 8.125 ps, the shear angle fell in the range of −17.8°–36.1°, and the peak occurred in the range of −8.8°–0.1°. In contrast, the shear angle of the side branch was 36.7°, and the shear angle of the primary ASB was 51.1°, shown as Fig.8(c-I). The shear angle of the maximum shear stress was oriented at a lower shear angle compared to that of the primary ASB and side-branch; this orientation induced atoms within the side-branch nucleation to deviate from the direction of the primary ASB. The shear angle deviation between the maximum shear stress and the primary ASB orientation might have been related to the superposition of the pressure and shear stress within the primary ASB. The superposition of the high pressure and shear stresses changed the direction of the maximum shear stress and drove the side-branch nucleation and wavy ASB formation. The ASB bifurcation phenomenon has been observed in Ti6Al4V [37] and other materials [38] through impact testing in previous studies.

3.2.4. Simultaneous activation of the two primary ASBs

When the machining speed reached 1300 m/s, the second-primary ASB occurred. The second-primary ASB nucleated at the free-surface corner, as Fig. 9. The primary ASB and the second-primary ASB were simultaneously active; this is illustrated by the von Mises stress field at 3.75 ps in Fig. 9(a). Subsequently, both the primary ASBs propagated and connected, as Figs. 9(b)–(d); this was the key material failure mode that prevented the primary ASB from reaching the free surface and prevented fragmented chip formation.

The onset of an ASB can be determined from the thermo- mechanical coupling of the ASB onset location. A theoretical description of the thermo- mechanical coupling of the ASB onset is present in the literature [39]. It is based on a partial differential system constructed using basic equations of solid mechanics. In 1982, Bai [40] proposed a criterion for ASB onset by applying the perturbation method to a partial differential

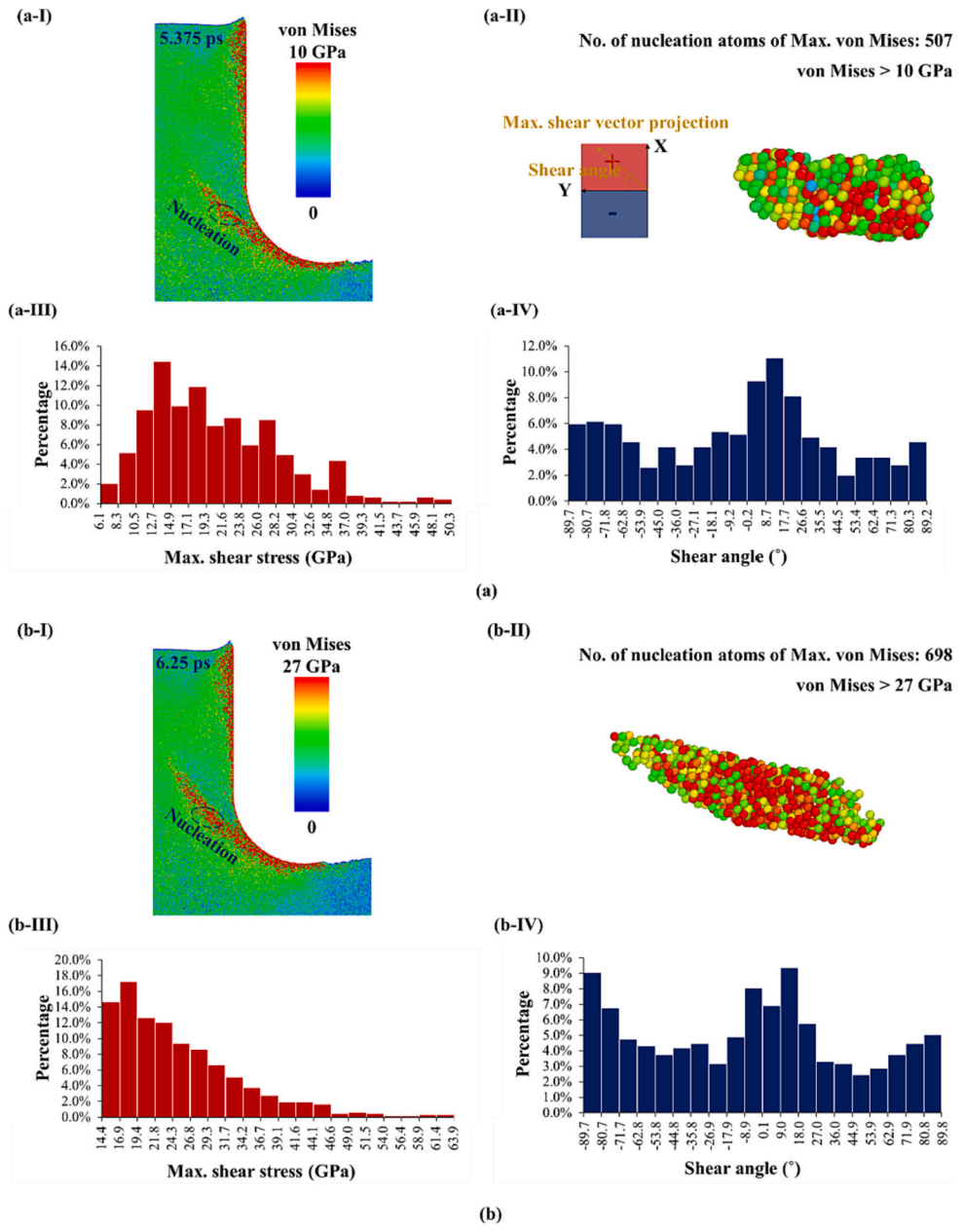

Fig. 8. Statistical analysis of the maximum shear stress and the corresponding direction of the atoms within the nucleation of the side branch; (a-I), (b-I), and (c-I) show the maximum shear stress field without averaging; (a-II), (b-II), and (c-II) show the atoms that satisfied the stress criteria; (a-III), (b-III), and (c-III) show the pressure distribution of the atoms shown in (a-II), (b-II), and (c-II), respectively; (a-IV), (b-IV), and (c-IV) show the direction of the maximum shear stress distribution of the atoms showing in (a-II), (b-II), and (c-II), respectively. The side branch should be induced by the disturbance of the localized high pressure that changes the orientation of the maximum shear stress.

system. The criterion is as follows:

$$\frac{\beta\tau\left(-\frac{\partial\tau}{\partial T}\right)}{\rho c_V \frac{\partial\tau}{\partial\gamma}} > 1, \tag{9}$$

where ρ is the material density; c_v is the volumetric heat capacity; and γ is the shear strain; τ is the shear stress oriented along the direction of the ASB, which is a function of the shear strain γ, shear strain rate $\dot{\gamma}$, and temperature T. The criterion described above implies that the ASB onset takes place when $\partial\tau/\partial T$ overwhelms $\partial\tau/\partial\gamma$. For most material, $\partial\tau/\partial T$ is a negative number, and the shear stress should sharply fall off at a high temperature between the room temperature and the melting point. In machining, the high temperature was induced by the plastic work conversion. Specifically, in Case 1 (200 m/s), the material in front of the cutter tip was under stress concentration that did plastic work resulting in accumulated heat. The accumulated heat elevates the localized temperature that is beneficial to the increase of $-\partial\tau/\partial T$ and decrease of $\partial\tau/\partial\gamma$, which further causes ASB.

As Figs. 9(e)–(h), the compression adjacent to the cutter-workpiece interface manifests. The compression was induced by the inertial force of the atoms that were sharply accelerated by the impact of the cutter. The impact simultaneously results in the localized shear stresses further causing the second-primary ASB and the minor ASBs to grow from the cutter-workpiece interface, as Figs. 9(a)–(d). Owing to the compliance of the surface material at the free-surface corner alleviating the localized

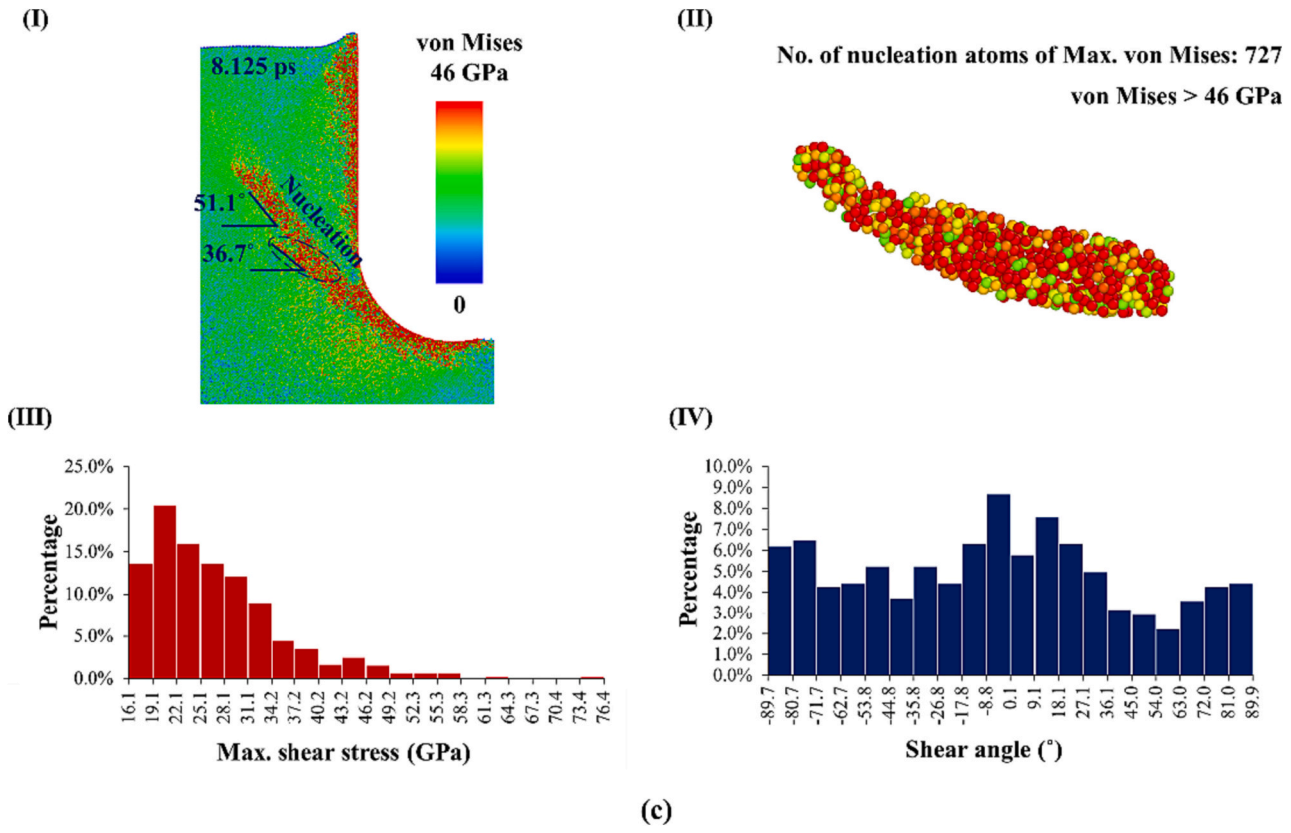

Fig. 8. (*continued*).

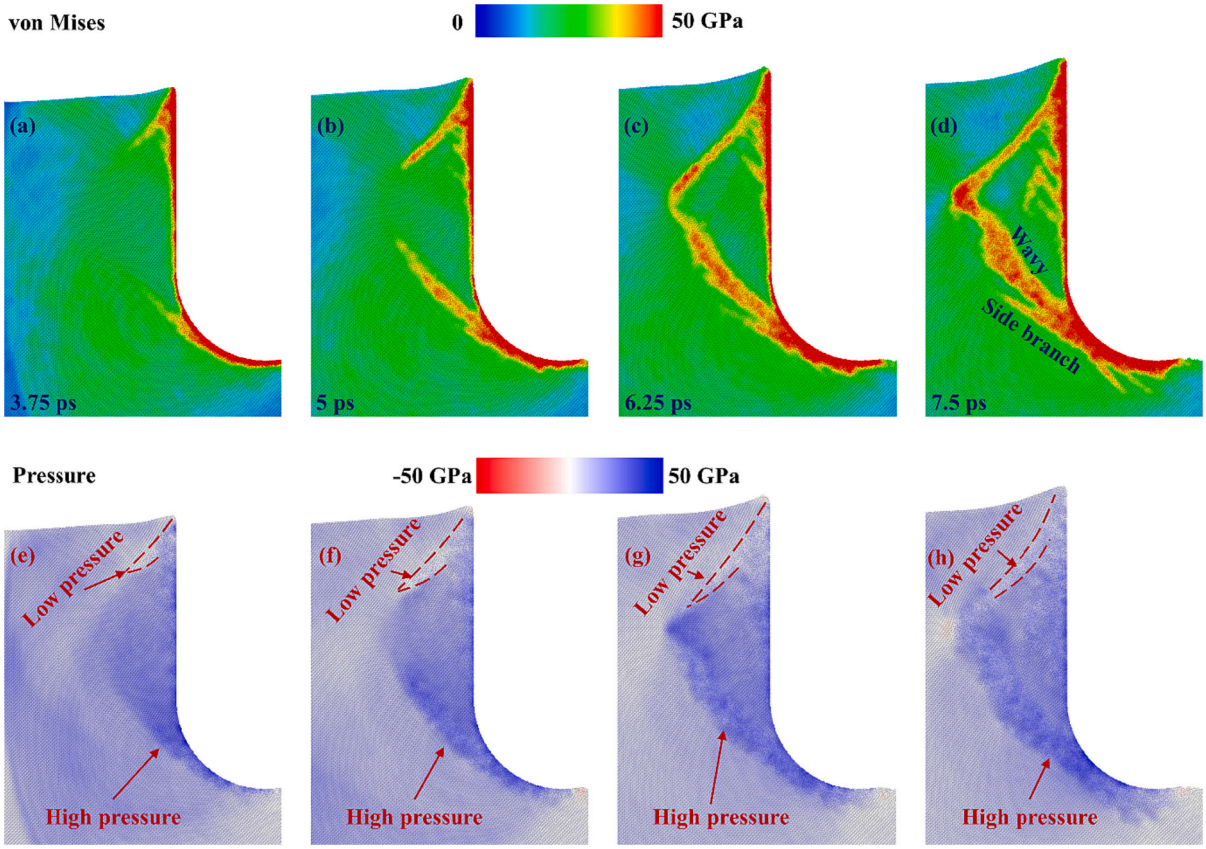

Fig. 9. The simultaneous onset and propagation of the two primary ASBs under the machining speed of $v_C = 1300$ m/s. The cut-off radius of the assumed sphere for von Mises and pressure averaging was 8 Å. The second-primary ASB was induced by the impacted materials adjacent to the cutter-material interface.

shear stress, the onset of the second-primary ASB requires higher machining speeds, compared with the machining speed only causing minor ASBs. This mechanism explains why only minor ASBs occurs in Case 2 (1086 m/s), and the second-primary ASB occurs in Case 3 with a higher machining speed (1300 m/s).

The influence of stress on the ASB onset can also be corroborated at the nanometer scale. In 2016, Zhao et al. [41] studied micro-ASB formation in SCS and suggested that the difference in Gibbs free energy between the crystalline and amorphous structures is caused by the energy barrier resisting the transformation from a crystalline structure to an amorphous structure; this energy barrier can be overcome by stress work and can be obtained using

$$\Delta G_{c-a}(T;P,\tau=0) = p\varepsilon_V + \tau\gamma + \Delta G_{c-a}(T;P,\tau), \tag{10}$$

where ΔG_{c-a} is the energy barrier that has to be surpassed to transition from the crystalline to amorphous phase. When the work done by the stress is sufficiently high, it satisfies the following condition: $\Delta G_{c-a}(T;P,\tau) = 0$; this initiates the transformation from a crystalline structure to an amorphous structure. For the ASB onset, the work done by the stress should be primarily provided by the shear stress. Eq. (10) can be used to obtain the amount of work required to activate the ASB onset. A large amount of work requires sufficiently high shear stress, which can be induced by a high machining speed.

3.3. The mechanism of failure modes governed by pressure

3.3.1. Shock wave attenuation and jetted chips driven by pressure

The shock wave began to attenuate after the cutter contacts the workpiece. The attenuation stage can be considered the transient state, which is followed by a steady state in which the machining processes are steady. The case under the machining speed of v_C = 5431 m/s was considered as an example to demonstrate the shock wave attenuation at the transient state and the pressure field at a steady state in UHSM. In the transient state, the shock wave propagated from the interface between the workpiece and rake face and formed a high-pressure region, as Fig. 10(a). Attenuation occurred in the first several picoseconds. After t = 2 ps, the width of the damage region was 170.45 Å. After 3 ps, the width of the damaged region reached 309.3 Å and remained at approximately 307 Å. Thus, the width of the high-pressure region increased in the first 5 ps and remained constant thereafter. The material response after 6 ps was in the transient state, and a steady state was achieved after 6 ps. In the transient state, the shock wave attenuated, causing the pressure to decrease and the width of the high-pressure region to increase. Once a steady state was achieved, the pressure field

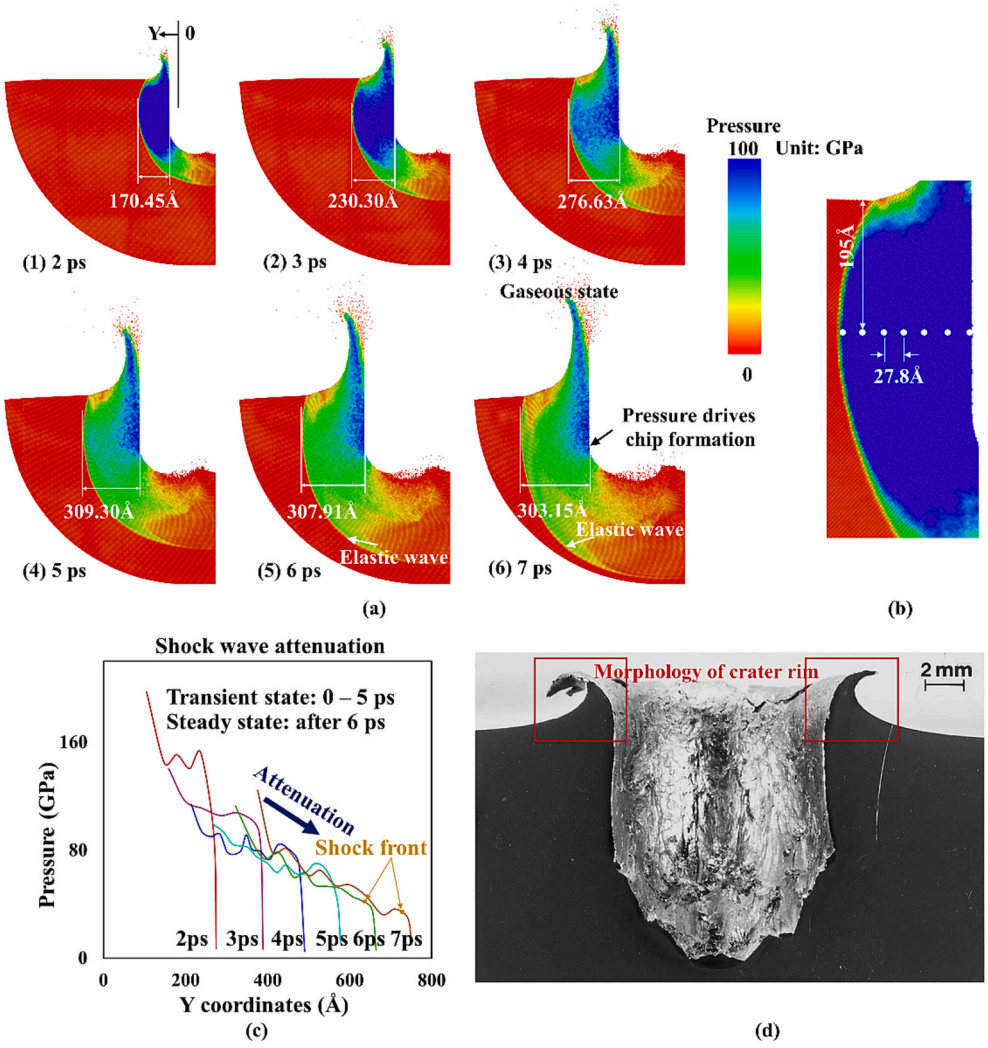

Fig. 10. The process of jetted chip formation and shock wave attenuation; (a) shows the chip formation process driven by pressure; the machining speed was v_C = 5431 m/s. The cut-off radius of the assumed sphere for pressure averaging was 8 Å. (b) shows the pressure measurement process; (c) shows the measured stress at distinct moments during the shock wave attenuation process; (d) shows the morphology of the rim of a crater caused by the impact from a projectile of stainless steel with the speed of 3000 m/s [42]. The target is 1100-type aluminum. The morphology of the rim and the jetted chips are similar.

stabilized. The pressure at several points within the high-pressure region was measured to quantitatively present the pressure distribution in the high-pressure region. The measurement points were evenly distributed in a line with an interval of 27.8 Å, and the distance between the free surface and the measurement line was 195 Å, as Fig. 10(b). The measured pressures are shown in Fig. 10(c), wherein it can be seen that the pressure decreased in the first 5 ps, which shows the shock wave attenuation occurred within the first 5 ps. Subsequently, the pressure became stable, which implies a steady state was achieved. Because the highest pressure was at the interface of the workpiece and the rake face, the localized pressure drove the material to jet to the free-surface side where the lower pressure region was located, as Fig. 10(a). In other words, the formation of the jetted chips was driven by the pressure gradient. The jetted-chip morphology is similar to the crater-rim morphology in the crater-impacting experiments conducted by Murr et al. [42]. In the experiments, 1100-type aluminum was impacted by a stainless-steel projectile with the shape of sphere. The diameter of the sphere is 3.18 mm. The impact speed of 3000 m/s causes the high pressure in the target driving the crater-rim material to jet. For comparison, the characterization of the crater-rim morphology was presented in Fig.10(d). Additionally, as Fig. 10(a), many atoms vaporized from the surface of the jetted chips and formed a gaseous state. Owing to the article limit, the vaporization will not be discussed in details.

3.3.2. *The relation of variables at transient state*

In the transient state of UHSM, variations in variables, including machining speed, shock wave speed, pressure, and compression ratio, are considered discontinuous processes in theory [20]; this is because the duration of these variations is too short. To demonstrate such a situation, a case with the machining speed of $v_C = 5431$ m/s was taken as an example. Fig. 11(a) illustrates the process of one atom experiencing the shock front of a shockwave. Within 0.1 ps, the shock front passed by the atom, and the shock wave elevated the pressure of the atom from 4 to 200 GPa; the process of the shock front passing by the atom was too short and difficult to study as a continuous process. Therefore, the process was treated as discontinuous and depicted by the Rankine-Hugoniot jump condition [20]. The Rankine-Hugoniot jump condition is constructed by three conservation laws. Thus, the variables, including pressure, machining speed, and shock wave speed, were treated as state quantities, and the variations in the process were ignored. Based on this theoretical framework, the relationship between the shock wave speed and the machining speed is shown in Fig. 11(b). It was observed that the transient shock wave speed monotonically increased with increasing machining speeds. If the machining speed is assumed to be the atom speed at the cutter-workpiece interface, then this monotonic increase can be described by the empirical relation EOS, which is given by $v_S = 1.03v_C + 7.22$ km/s through linear fitting. In addition, the relationship between the machining speed and pressure at the shock front was investigated; the results are plotted in Fig. 11(c), which also displays a monotonic increase. Hence, it can be concluded that the localized pressure induced by inertia drives the propagation of the shock wave. A higher localized pressure results in a higher shock-wave speed. A quantitative discussion on the relationship between the shock wave speed and pressure is presented in Section 3.3.3.

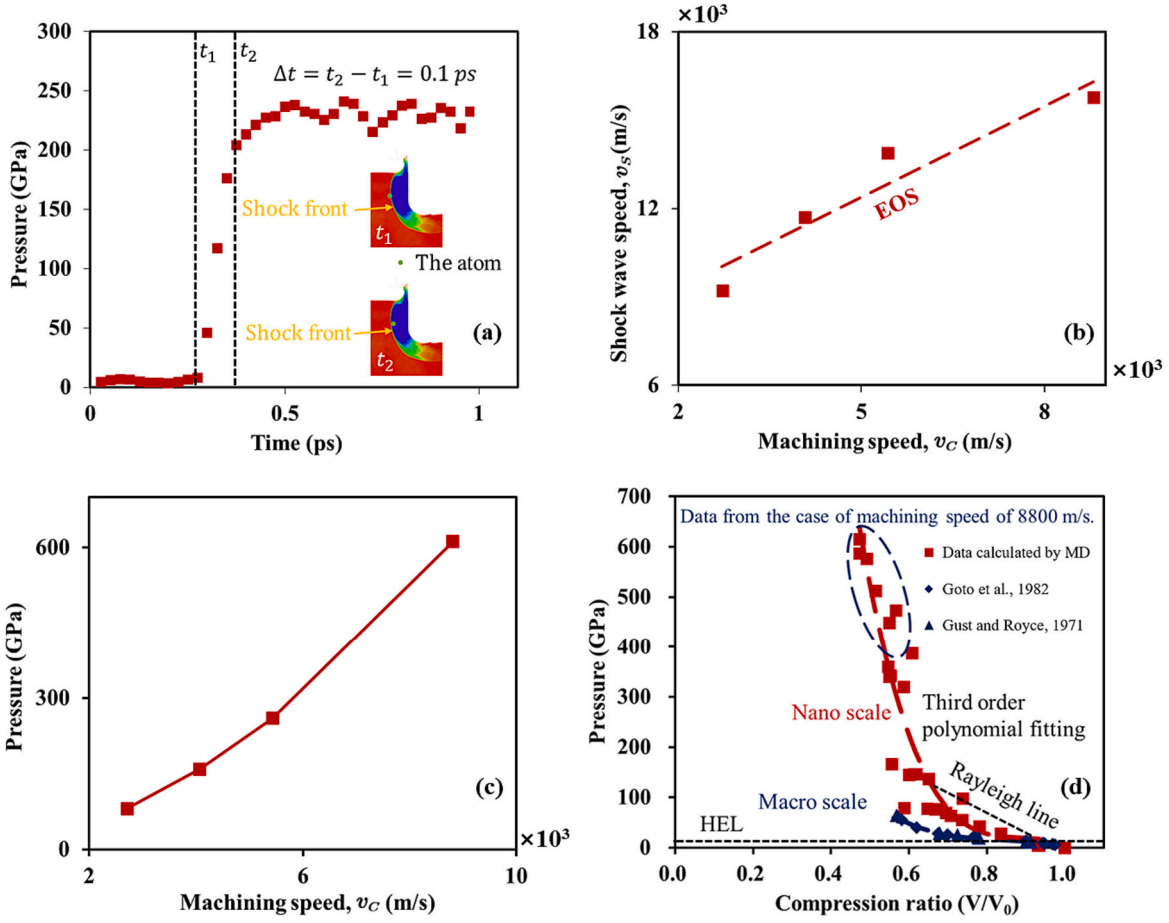

Fig. 11. The relationship among the variables at the transient state; (a) shows the pressure on the atom increased to 200 GPa during passing by a shock front within a short time (0.1 ps); The short time results in the jump-style increase of the pressure. (b) shows the relationship between the shock wave speed and machining speed at the transient state; (c) shows the relationship between the pressure and machining speed at the transient state; (d) shows the relation between the pressure and compression ratio that was established based on the Vonoroi tessellation algorithm.

Fig. 11(d) shows the pressure varied with the compression ratio. The pressure is plotted against the compression ratio as red squares in Fig. 11 (d) and fitted by a third-order polynomial. It was observed that high pressure resulted in a high compression ratio. The results were compared with the impact experimental results provided by Goto et al. [43] and Gust and Royce [44]. Based on the comparison, it was found that higher pressures occurred in MD simulations in the compression ratio range of 0.55–0.8; this range can be attributed to the fact that the MD simulation was conducted at the nanometer scale, which may have caused a "size effect" [45]. Additionally, the Hugoniot elastic limit was approximately 9–15 GPa at a compression ratio of 0.95, which is consistent with the results of the impact experiments.

3.3.3. Shock wave speed at steady state

Shock wave propagation was driven by the localized pressure in both the transient and steady states. Fig. 12 illustrates the transition from the transient state to the steady state under the machining speed of v_C = 2715 m/s; this case was selected as an example because the cases at higher machining speeds required longer time to achieve a steady state, which requires larger models to accommodate the longer time of machining.

In Fig. 12(a), the left side of the workpiece is set as the origin of the horizontal axis. The distance between the left side and cutter-workpiece interface is L_2; the distance between the left side and shock front is L_1; the damage region length is L. The variation in the damage region length is given by

$$\frac{dL}{dt} = \frac{dL_1}{dt} - \frac{dL_2}{dt} = v_S - v_C. \tag{11}$$

Because the volumetric compression in the high-pressure region was

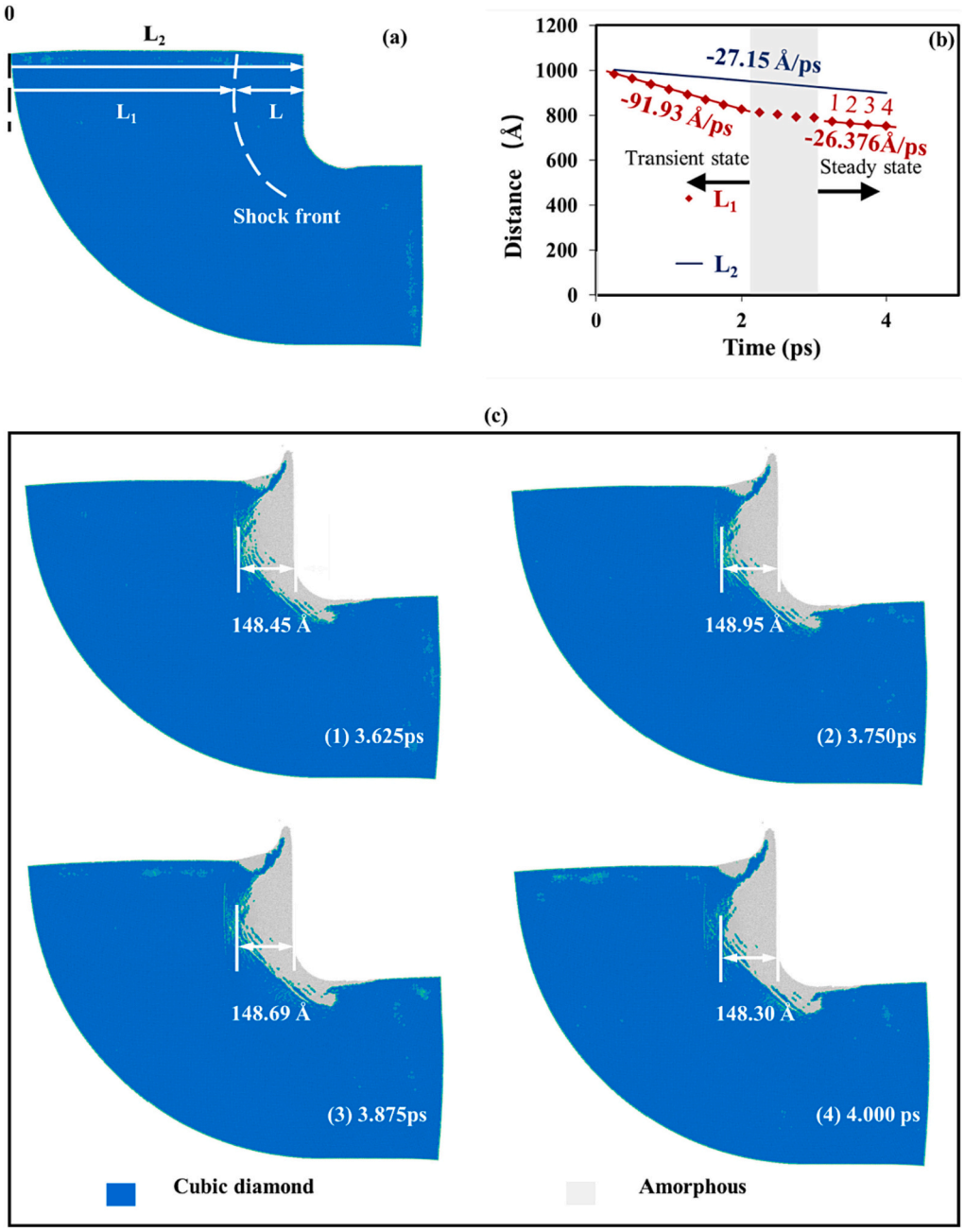

Fig. 12. Shock wave speed transitions from the transient state to the steady state under the condition of v_C = 2715 m/s. The transient state is followed by a steady state. At transient sate, shock wave speed is higher than the machining speed; at steady state, shock wave is equal to the machining speed.

caused by the cutter thrust along the machining direction, the volumetric compression ratio within the high-pressure region can be assumed to be equal to the length compression ratio along the machining direction. Then, the width of the high-pressure region is related to the width of the high-pressure material under free status as

$$L = \frac{V}{V_0} L_0, \tag{12}$$

where V_0 is the specific volume of the damaged region at free status; and L_0 is the width of the damaged region at free status. Another relationship that requires consideration is the conservation relationship. According to the mass and momentum conservation at the shock front governed by the Rankine-Hugoniot jump condition, the shock wave speed is given by [20]

$$v_S = \frac{1}{\rho_0}\sqrt{-\frac{p-p_0}{V-V_0}}, \tag{13}$$

where p is the pressure at an arbitrary state after starting machining; and p_0 is the pressure at the initial state. Note that Eq. (13) can be used to describe the shock wave speed at transient state. Combining Eqs. (12) and (13), an equation regarding the width of the high-pressure region in terms of the pressure and shock wave speed is given by

$$L = L_0\left[1 - \frac{1}{V_0}\frac{p-p_0}{V_0(v_S\rho_0)^2}\right]. \tag{14}$$

The derivative of Eq. (14) with respect to time can be written as follows.

$$\frac{dL}{dt} = -\frac{L_0}{V_0}\left[\frac{1}{(v_S\rho_0)^2}\frac{dp}{dt} - 2(p-p_0)v_S^{-3}\rho_0^{-2}\frac{dv_S}{dt}\right]. \tag{15}$$

From the equation above, it can be inferred that pressure p decreases with time in the transient state and remains constant in the steady state, which can be confirmed from Fig. 10(a). The shock velocity must be constant at a steady state under constant machining velocity. Therefore, in the steady state, two relations should exist:

$$\frac{dp}{dt} = 0 \text{ and } \frac{dv_S}{dt} = 0. \tag{16}$$

Substituting Eq. (16) into Eq. (15), the following relation is obtained:

$$\frac{dL}{dt} = 0. \tag{17}$$

Based on Eqs. (11) and (17), it can be concluded that the shock wave speed should be equal to the machining speed at the steady state ($v_S = v_C$); this conclusion is consistent with the results of the MD simulation shown in Fig. 10(b), which shows the variations in the distance L_1 and L_2 with time. The slopes of L_1 and L_2 are the shock wave speed and the machining speed, respectively. In the transient state, L_1 had a larger slope, which shows that the shock wave speed was faster than the machining speed. At the steady state, the slope of L_1 was −27.15 Å/ps and parallel to the slope of L_2, which shows that the shock wave speed was equal to the machining speed. The width of the high-pressure region at four moments in the steady state, marked by the four points in Fig. 12(b), is illustrated in Fig. 12(c). The width was approximately 148 Å in the steady state, which shows that the shock wave speed was equal to the machining speed and consistent with Eq. (17).

Combining the transient state and the steady state, the shock wave speed is given by

$$v_S = \begin{cases} \frac{1}{\rho_0}\sqrt{-\frac{p-p_0}{V-V_0}} & \textit{transient state} \\ v_C & \textit{steady state} \end{cases}$$

This conclusion is different from the previous conclusion that states the machining speed was larger than the plastic wave speed [18,19,46] when the machining speed was elevated to a critical value. In the previous conclusion, the plastic wave speed was derived from the plastic part of the stress-strain curve of the workpieces. However, the simulations showed no plastic shear wave at the machining speeds at which the shear stress governed the material failure modes. In these cases, the energy emitted from the cutter was consumed by the ASBs, and only a few elastic waves propagated to deep locations. Furthermore, the simulations showed that when the machining speed increased to higher levels at which the pressure governed the material failure modes, the shock waves occurred. The shock wave speed can be derived from Rankine-Hugoniot relation or calculated based on the curve representing the relation between pressure and specific volume as Fig. 11(d).

4. Conclusions

In this study, to explore the failure mode of SCS at different machining speeds, MD simulations were conducted. The results from the MD simulations were analyzed based on the current theoretical framework and some phenomena in the impacting experiments. The following conclusions were drawn.

- The MD simulations suggested that when the machining speed is higher than that causing fragmented chips, jetted chips should exist. Furthermore, the pressure induced by atom inertia in front of the rake face is the primary cause of jetted chip formation. The transition from fragmented chips to jetted chips experiences a stage wherein two primary ASBs simultaneously onset and propagate.
- No plastic/shock wave were observed in the machining speed range in which the shear stress governed the material failure mode. The shock wave speed was higher than the machining speed at transient state, which can be described by the EOS. In addition, the shock wave speed was proved to be equal to the machining speed in the steady state. The Rankine-Hugoniot jump condition was introduced to elucidate the shock wave speed.
- When shear stress governs material deformation behavior, the shear strain played a significant role in heat generation, and the highest temperature occurs within ASB. In the case of machining speeds at 200 m/s, the larger shear strain causes the higher temperature compared with other cases of machining speed lower than 1300 m/s. For the cases of machining speeds at 2000 m/s and 2715 m/s, the location of high temperatures transited from ASBs to high-pressure region. At machining speeds higher than 4073 m/s, the pressure and volumetric strain became the primary factor contributing to heat generation, which causes the maximum temperature in the high-pressure region.

Supplementary data to this article can be found online at https://doi.org/10.1016/j.jmapro.2023.09.064.

Declaration of competing interest

The authors declare the following financial interests/personal relationships which may be considered as potential competing interests: Bi Zhang reports financial support was provided by Shenzhen Science and Technology Innovation Committee.

Acknowledgement

The authors would like to thank the financial support from the Peacock Program of Shenzhen (KQTD20190929172505711), the project numbered JSGG20210420091802007 from Shenzhen Science and Technology Innovation Commission of China, and the project numbered 2021B1515120009 from Guangdong Province. We aslo need to thank the support from the Center for Computational Science and Engineering affiliated to Southern University of Science and Technology.

References

[1] Burns TJ, Davies MA. On repeated adiabatic shear band formation during high-speed machining. Int J Plast 2002;18:487–506. https://doi.org/10.1016/S0749-6419(01)00006-7.

[2] Komanduri R, Schroeder T, Hazra J, von Turkovich BF, Flom DG. On the catastrophic shear instability in high-speed machining of an AISI 4340 steel. J Eng Ind 1982;104:121–31. https://doi.org/10.1115/1.3185807.

[3] Sutter G, List G. Very high speed cutting of Ti–6Al–4V titanium alloy–change in morphology and mechanism of chip formation. Int J Mach Tool Manuf 2013;66:37–43.

[4] Ye GG, Xue SF, Ma W, Jiang MQ, Ling Z, Tong XH, et al. Cutting AISI 1045 steel at very high speeds. Int J Mach Tool Manuf 2012;56:1–9. https://doi.org/10.1016/j.ijmachtools.2011.12.009.

[5] Ye GG, Xue SF, Jiang MQ, Tong XH, Dai LH. Modeling periodic adiabatic shear band evolution during high speed machining Ti-6Al-4V alloy. Int J Plast 2013;40:39–55. https://doi.org/10.1016/j.ijplas.2012.07.001.

[6] Molinari A, Soldani X, Miguélez MH. Adiabatic shear banding and scaling laws in chip formation with application to cutting of Ti–6Al–4V. J Mech Phys Solids 2013;61:2331–59. https://doi.org/10.1016/j.jmps.2013.05.006.

[7] Huang Y, Liang SY. Cutting forces modeling considering the effect of tool thermal property—application to CBN hard turning. Int J Mach Tool Manuf 2003;43:307–15.

[8] Mitrofanov AV, Babitsky VI, Silberschmidt VV. Finite element analysis of ultrasonically assisted turning of Inconel 718. J Mater Process Technol 2004;153:233–9.

[9] Shrot A, Bäker M. Determination of Johnson–Cook parameters from machining simulations. Comput Mater Sci 2012;52:298–304.

[10] Trimble D, Agarwal A, McDonnell D, Barron S, Ahearne E, O'Donnell GE. Finite element simulation of orthogonal machining of biomedical grade Co–Cr–Mo alloy. CIRP J Manuf Sci Technol 2020;28:8–14. https://doi.org/10.1016/j.cirpj.2020.01.008.

[11] Ma W, Li X, Dai L, Ling Z. Instability criterion of materials in combined stress states and its application to orthogonal cutting process. Int J Plast 2012;30–31:18–40. https://doi.org/10.1016/j.ijplas.2011.09.003.

[12] Abdulkadir LN, Abou-El-Hossein K, Jumare AI, Liman MM, Olaniyan TA, Odedeyi PB. Review of molecular dynamics/experimental study of diamond-silicon behavior in nanoscale machining. Int J Adv Manuf Technol 2018;98:317–71. https://doi.org/10.1007/s00170-018-2041-7.

[13] Goel S, Luo X, Agrawal A, Reuben RL. Diamond machining of silicon: a review of advances in molecular dynamics simulation. Int J Mach Tool Manuf 2015;88:131–64. https://doi.org/10.1016/j.ijmachtools.2014.09.013.

[14] Salomon CJ. Process for machining metals of similar acting materials when being worked by cutting tools. 1931, 523594.

[15] Longbottom JM, Lanham JD. A review of research related to Salomon's hypothesis on cutting speeds and temperatures. Int J Mach Tool Manuf 2006;46:1740–7. https://doi.org/10.1016/j.ijmachtools.2005.12.001.

[16] Shaw MC, Cookson JO. Metal cutting principlesvol. 2. New York: Oxford University Press; 2005.

[17] Sutter G, Ranc N. Flash temperature measurement during dry friction process at high sliding speed. Wear 2010;268:1237–42.

[18] Zhou L, Shimizu J, Muroya A, Eda H. Material removal mechanism beyond plastic wave propagation rate. Precis Eng 2003;27:109–16. https://doi.org/10.1016/S0141-6359(02)00124-1.

[19] Wang B, Liu Z, Su G, Song Q, Ai X. Investigations of critical cutting speed and ductile-to-brittle transition mechanism for workpiece material in ultra-high speed machining. Int J Mech Sci 2015;104:44–59. https://doi.org/10.1016/j.ijmecsci.2015.10.004.

[20] Meyers MA. Dynamic behavior of materials. John Wiley & Sons. 1994.

[21] Berendsen HJ, van Postma J, Van Gunsteren WF, DiNola A, Haak JR. Molecular dynamics with coupling to an external bath. J Chem Phys 1984;81:3684–90.

[22] Tersoff J. Chemical order in amorphous silicon carbide. Phys Rev B 1994;49:16349.

[23] Thompson AP, Plimpton SJ, Mattson W. General formulation of pressure and stress tensor for arbitrary many-body interaction potentials under periodic boundary conditions. J Chem Phys 2009;131:154107.

[24] Guan Y, Song W, Wang Y, Liu S, Yu Y. Dynamic responses in shocked Cu-Zr nanoglasses with gradient microstructure. Int J Plast 2022;149:103154. https://doi.org/10.1016/j.ijplas.2021.103154.

[25] Hahn EN, Germann TC, Ravelo R, Hammerberg JE, Meyers MA. On the ultimate tensile strength of tantalum. Acta Mater 2017;126:313–28. https://doi.org/10.1016/j.actamat.2016.12.033.

[26] Maras E, Trushin O, Stukowski A, Ala-Nissila T, Jónsson H. Global transition path search for dislocation formation in Ge on Si(001). Comput Phys Commun 2016;205:13–21. https://doi.org/10.1016/j.cpc.2016.04.001.

[27] Hansen J-P, McDonald IR. Theory of simple liquids. Phys Today 1988;41:89–90.

[28] Cai SL, Dai LH. Suppression of repeated adiabatic shear banding by dynamic large strain extrusion machining. J Mech Phys Solids 2014;73:84–102. https://doi.org/10.1016/j.jmps.2014.09.004.

[29] Fortner J, Lannin JS. Radial distribution functions of amorphous silicon. Phys Rev B 1989;39:5527.

[30] Laaziri K, Kycia S, Roorda S, Chicoine M, Robertson JL, Wang J, et al. High resolution radial distribution function of pure amorphous silicon. Phys Rev Lett 1999;82:3460.

[31] Zhao S, Kad B, Hahn EN, Remington BA, Wehrenberg CE, Huntington CM, et al. Pressure and shear-induced amorphization of silicon. Extreme Mech Lett 2015;5:74–80. https://doi.org/10.1016/j.eml.2015.10.001.

[32] Ye GG, Jiang MQ, Xue SF, Ma W, Dai LH. On the instability of chip flow in high-speed machining. Mech Mater 2018;116:104–19. https://doi.org/10.1016/j.mechmat.2017.02.006.

[33] Xu Y, Zhang J, Bai Y, Meyers MA. Shear localization in dynamic deformation: microstructural evolution. Metall Mater Trans A 2008;39:811–43.

[34] Huang Y. Accurate dilatation rates for spherical voids in triaxial stress fields. J Appl Mech Trans ASME 1991;58:1084–6.

[35] Rice JR, Tracey DM. On the ductile enlargement of voids in triaxial stress fields. J Mech Phys Solids 1969;17:201–17.

[36] Wang B, Liu Z. Evaluation on fracture locus of serrated chip generation with stress triaxiality in high speed machining of Ti6Al4V. Mater Des 2016;98:68–78. https://doi.org/10.1016/j.matdes.2016.03.012.

[37] Sun K, Yu X, Tan C, Ma H, Wang F, Cai H. Effect of microstructure on adiabatic shear band bifurcation in Ti–6Al–4V alloys under ballistic impact. Mater Sci Eng A 2014;595:247–56.

[38] Yang Y, Jiang L. Self-organization of adiabatic shear bands in ZK60 Magnesium alloy. Mater Sci Eng A 2016;655:321–30.

[39] Wright TW. The physics and mathematics of adiabatic shear bands. Cambridge University Press; 2002.

[40] Bai YL. Thermo-plastic instability in simple shear. J Mech Phys Solids 1982;30:195–207. https://doi.org/10.1016/0022-5096(82)90029-1.

[41] Zhao S, Hahn EN, Kad B, Remington BA, Wehrenberg CE, Bringa EM, et al. Amorphization and nanocrystallization of silicon under shock compression. Acta Mater 2016;103:519–33. https://doi.org/10.1016/j.actamat.2015.09.022.

[42] Murr LE, Quinones SA, Ferreyra TE, Ayala A, Valerio OL, Hörz F, et al. The low-velocity-to-hypervelocity penetration transition for impact craters in metal targets. Mater Sci Eng A 1998;256:166–82. https://doi.org/10.1016/S0921-5093(98)00796-5.

[43] Goto T, Sato T, Syono Y. Reduction of shear strength and phase-transition in shock-loaded silicon. Jpn J Appl Phys 1982;21:L369.

[44] Gust WH, Royce EB. Axial yield strengths and two successive phase transition stresses for crystalline silicon. J Appl Phys 1971;42:1897–905.

[45] Gao H, Huang Y, Nix WD, Hutchinson JW. Mechanism-based strain gradient plasticity — I. Theory. J Mech Phys Solids 1999;47:1239–63. https://doi.org/10.1016/S0022-5096(98)00103-3.

[46] Wang B, Liu Z, Cai Y, Luo X, Ma H, Song Q, et al. Advancements in material removal mechanism and surface integrity of high speed metal cutting: a review. Int J Mach Tool Manuf 2021;166:103744. https://doi.org/10.1016/j.ijmachtools.2021.103744.